Computational Molecular Analysis of Chloride Transport in Hydrated Cement Paste

Tongyan Pan and Yajun Liu

Concrete in transportation infrastructure is constantly subjected to the ingress of chloride, which could cause reinforcement corrosion and significant deterioration of concrete structures if not well controlled. Major types of reinforcement corrosion, such as pitting corrosion and concentration-cell corrosion, are usually initiated with localized chloride concentrations whose behavior is closely related to the transport characteristics of chloride ions in hydrated cement paste. However, unless studied at the molecular level, chloride transport behavior cannot be properly understood and controlled in view of the high heterogeneity of cement paste. The findings are presented from a research study recently conducted with a molecular dynamics (MD) approach to investigate the physicochemical nature of the various interactions between chloride ions and cement hydration products, which might significantly influence chloride transport in cement paste. Six hydrated compounds including portlandite, C-S-H phases (tobermorite and jennite), AFm phases (hydrocalumite and kuzelite), and the AFt phase (ettringite) were modeled and then validated by using the ^{35}Cl nuclear magnetic resonance spectroscopy technique. On the basis of the MD-generated ionic trajectory, the macroscopic transport phenomenon of chloride species was evaluated in the vicinity of each different hydration product in terms of a computed effective diffusion coefficient.

Portland cement concrete possesses superior robustness and impact resistance, making it a material of choice for transportation infrastructure, mainly highway and airport pavement slabs, bridge decks, and street surfaces. As a porous and highly heterogeneous composite, the concrete used in transportation infrastructure, however, is inevitably subjected to the ingress of chloride from various external sources such as winter anti-icing and deicing activities, chloride-laden marine environments, and, less frequently, certain construction practices such as the use of calcium chloride as a concrete setting accelerator (*1*). Excessive accumulation of chloride could cause reinforcement corrosion that, if not well controlled, would lead to significant reduction in the strength, serviceability, and aesthetics of concrete structures (*2*).

The current status of knowledge on chloride transport in concrete is built predominantly on the bulk properties of concrete including concrete permeability and species diffusivity (*3*). The concrete matrix, however, is well known to be highly heterogeneous, consisting of various ingredients with different physicochemical properties that could interact with chloride ions in different ways. Chemical bonding or physical attraction to certain cement hydration products could significantly influence the transport of chloride ions and lead to different concentration distributions from that predicted by continuum-based approaches. According to a recent U.S. nationwide survey, locally concentrated chloride ions have been found to be closely related to the two major types of reinforcement corrosion occurring in concrete bridge decks: pitting corrosion and concentration-cell corrosion (*4*).

Within this context, a research study was recently initiated to investigate the transport behavior of chloride in the heterogeneous concrete matrix by using a multiscale approach. This study targets an improved understanding and a more accurate prediction of chloride transport in concrete, to be achieved in a bottom-up mode starting from exploration of the physicochemical behavior of chloride ions in the vicinity of solid hydration products by using molecular dynamics (MD) analysis. The findings from the MD analysis task of the study are presented, with a focus on the transport behavior of chloride ions in the representative hydration phases of ordinary calcium silicate and calcium aluminate cements.

PHYSICOCHEMISTRY OF HYDRATED CEMENT PASTE

Research at the molecular level has offered strong arguments that the cohesion of primary hydration products—$Ca(OH)_2$, C-S-H, AFt, and AFm—all attribute to short- and medium-range forces on migrating species (*5*). The forces acting on migrating chloride ions in cement paste are either physically natured or more chemically oriented. From the existing knowledge of the physicochemistry of hydrated cement paste, studying the behavior of chloride ions at the atomic level is envisioned as shedding light on the phenomena that cannot be explained by using the bulk-materials-based approaches, such as reinforcement corrosion due to chloride concentration (*6*). With advances in computer technology, recent years have seen successful MD applications in simulating the physicochemical behavior of fundamental entities including atoms, ions, and molecules as well as in studying the complex dynamic processes in chemistry and physics. More meaningful to the subject of this study, MD simulations have been used to study the phenomenon of species binding to the C-S-H phases of cement paste, and results have generally agreed with the experimental adsorption results from nuclear magnetic resonance (NMR) spectroscopy analyses (*7*).

Western Transportation Institute, Montana State University, P.O. Box 174250, Bozeman, MT 59717-4250. Corresponding author: T. Pan, tongyan.pan@coe.montana.edu.

Transportation Research Record: Journal of the Transportation Research Board, No. 2113, Transportation Research Board of the National Academies, Washington, D.C., 2009, pp. 31–40.
DOI: 10.3141/2113-04

FUNDAMENTALS OF MD ANALYSIS

The concept of MD simulation was first introduced by Alder and Wainwright to study the phase diagram of a hard sphere system in the late 1950s (*8, 9*), followed by Rahman and Stillinger, who conducted pioneering work to simulate the realistic potential for liquid argon and liquid water (*10, 11*). An MD simulation includes four integral components—the potential function to compute the forces among the microscopic entities, the classical mechanics to determine the acceleration and instantaneous velocity of entities, the statistical mechanics to compute the macroscopic thermodynamic observables, and the integration algorithm to solve for the trajectory and subsequently update the potential among the entities. The specific formats of the four components as used in this study are introduced briefly.

Potential Function

For the potential energy of the simulated chloride ion–cement paste system, as given in Equation 1, the first term is an electrostatic term for all Coulomb interactions between atomic charges and the second is a Lennard–Jones term to model the van der Waals interactions:

$$\phi = \sum_{ij}\left\{\frac{q_i q_j}{4\pi\epsilon_0 r_{ij}} + 4\epsilon_{ij}\left[\left(\frac{\sigma_{ij}}{r_{ij}}\right)^{12} - \left(\frac{\sigma_{ij}}{r_{ij}}\right)^{6}\right]\right\} \quad (1)$$

where

r_{ij} = distance between atoms i and j,
q_i, q_j = electrical charges centered on these atoms,
σ_{ij}, ϵ_{ij} = parameters of Lennard–Jones interaction potential, and
ϵ_0 = dielectric permittivity of vacuum (8.85419×10^{-12} F/m or $C^2N^{-1}m^{-2}$).

The term $(\sigma/r)^{12}$ in the Lennard–Jones term originates from the Pauli principle, which predicts an abrupt energy increase of a system when the electronic clouds surrounding the atoms start to overlap. The term $(\sigma/r)^6$ originates from the van der Waals dispersion forces as the dipole–dipole interactions among fluctuating dipoles. The Lennard–Jones parameters of interactions between different atomic species are determined according to the arithmetic combining as follows:

$$\sigma_{ij} = \frac{\sigma_{ii} + \sigma_{jj}}{2} \qquad \epsilon_{ij} = \sqrt{\epsilon_{ii}\epsilon_{jj}} \quad (2)$$

Classical Mechanics

In the MD analyses, the interatomic forces are determined as the gradient of the specified potential energy:

$$F_i = -\nabla_i \phi \quad (3)$$

where F_i is the force exerted on atom i.

The acceleration of the individual entities is then determined on the basis of Newton's equation of motion (Second Law):

$$F_i = m_i a_i \quad (4)$$

where m_i is the mass of particle i and a_i is the acceleration of atom i.

Newton's equation of motion used in the MD analyses takes the format of Equation 5 by combining Equations 3 and 4 to relate the derivative of the potential energy directly to the changes in positions of atoms (trajectory) as a function of time:

$$-\frac{d\phi}{dr_i} = m_i \frac{d^2 r_i}{dt^2}$$

or

$$a_i = \frac{d^2 r_i}{dt^2} = -\frac{1}{m_i}\frac{d\phi}{dr_i} \quad (5)$$

The initial positions of the atoms as used in this study come from previously determined material structures from the literature. The initial distribution of velocities was chosen randomly by using the Maxwell–Boltzmann distribution (Equation 6), which gives the probability that an atom i (with mass of m_i) has a velocity v_{ix} in the x-direction at a given temperature T:

$$f(v_{ix}) = \left(\frac{m_i}{2\pi k_B T}\right)^{1/2} \exp\left[-\frac{1}{2}\frac{m_i v_{ix}^2}{k_B T}\right] \quad (6)$$

where $f(v_{ix})$ is the probability density function and k_B is the Boltzmann constant.

Statistical Mechanics

In this study, statistical mechanics is used to monitor the specified temperature (298 K) based on the specified number of atoms and volume of each model. The temperature T is computed as the system average temperature $\langle T\rangle_{system}$ according to Equation 7, where $T(p^N, r^N)$ is the temperature, expressed as a function of the momenta p and the positions r. The integration is over all variables of r and p with the probability density of the system as given by

$$p(p^N, r^N) = \frac{1}{Q}\exp\left[-\frac{H(p^N, r^N)}{k_B T}\right]$$

where

H = Hamiltonian,
T = specified temperature (298 K), and
Q = partition function according to Equation 8.

$$\langle T\rangle_{system} = \int\int T(p^N, r^N)\rho(p^N, r^N)\cdot dp^N dr^N \quad (7)$$

$$Q = \int\int \exp\left[-\frac{H(p^N, r^N)}{k_B T}\right]\cdot dp^N dr^N \quad (8)$$

Considering that it would be too complicated to integrate the partition function Q for all possible states of the system, in this study the time average $\langle T\rangle_{time}$ of the system was determined and used as the system average $\langle T\rangle_{system}$ based on the ergodic hypothesis as follows:

$$\langle T\rangle_{time} = \lim_{\tau\to\infty}\frac{1}{\tau}\int_{t=0}^{\tau} T(p^N(t), r^N(t))\cdot dt \approx \frac{1}{M}\sum_{t=1}^{M} T(p^N, r^N) \quad (9)$$

where

parameter τ = simulation time,
$T(p^N(t), r^N(t))$ = instantaneous value of $T(p^N, r^N)$, and
M = number of time steps in the MD simulation.

Integration Algorithm

The integration algorithm is used to solve the trajectory (velocity and position) and subsequently update the potential among the entities. The potential energy is a function of the atomic positions of all the atoms (degrees of freedom = 3N) in the three-dimensional systems of this study, which is solved numerically by using Beeman's algorithm (*12*):

$$r(t+\delta t) = r(t) + v(t)\delta t + \frac{2}{3}a(t)\delta t^2 - \frac{1}{6}a(t-\delta t)\delta t^2$$

$$v(t+\delta t) = v(t) + \frac{7}{6}a(t)\delta t - \frac{1}{6}a(t-\delta t)\delta t \quad (10)$$

where

r = position,
v = velocity, and
a = acceleration.

Beeman's algorithm has the advantage of providing a more accurate expression for the velocities and better energy conservation.

MD MODELING OF CHLORIDE TRANSPORT IN HYDRATED CEMENT PASTE

Hydrated cement paste is well known as a mixture of four major types of hydration products: $Ca(OH)_2$, C-S-H, AFt, and AFm, with smaller amounts of hydrogarnet products. The composition of each major hydration product, especially the phases of C-S-H, AFt, and AFm, is highly heterogeneous. As such, the MD analysis of the heterogeneous cement paste as targeted in this study started with modulizing the inhomogeneous cement paste into individual products that each have a unique and well-determined crystalline structure. The overall transport behavior of the heterogeneous cement paste can then be properly obtained by synthesizing the individual modules based on their volumetric fractions in the overall paste system.

Portlandite presents a unique phase in cement paste and was modeled in this study on the basis of the crystal structure of $Ca(OH)_2$. Comprehensive C-S-H models proposed to represent phases of different Ca:Si ratios usually consist of tobermorite and jennite mixed with portlandite (*13*). Accordingly, tobermorite and jennite were modeled as the two basic crystalline structures on the basis of which more generic C-S-H phases can be studied. The Cl^- containing layered double hydroxide (LDH), hydrocalumite (Friedel's salt) and the SO_4^{2-} containing LDH–kuzelite are among the few AFm ingredients with a determined crystalline structure. As common AFm phases, they were modeled in this study to represent the AFm phases. Ettringite as the predominant AFt phase in concrete was selected as the representative model of the AFt phase in hydrated cement (*14*).

Portlandite Model

The portlandite phase [$Ca(OH)_2$] that occurs in hydrated cement has a relatively simple structure (*15*). The hexagonal-shaped unit cell of portlandite is given in Figure 1*a* with side lengths of $a = b = 3.585$ Å and $c = 4.895$ Å and angles of $\alpha = 90°$, $\beta = 90°$, and $\gamma = 120°$. The MD simulation model for portlandite contains $8 \times 4 \times 4$ crystallographic unit cells in the x-, y-, and z-directions of the Cartesian coordinate system, respectively (Figure 1*b*). The three-dimensional periodic boundary conditions (*16*) were applied to the model. Also shown (Figure 1*b*) is a layer of 495 water molecules above the four layers of unit cells of portlandite. The model simulates the water–portlandite system at a room temperature of 25°C (298 K) with a water density of 0.997 g/cm^3 and portlandite density of 1.419 g/cm^3. Notably, with the periodic boundary condition applied, the simulation model in Figure 1*b* can be perceived as having another four layers of unit cells of portlandite above the water molecule layer; therefore this model actually simulates a 40-Å-diameter portlandite channel filled with water.

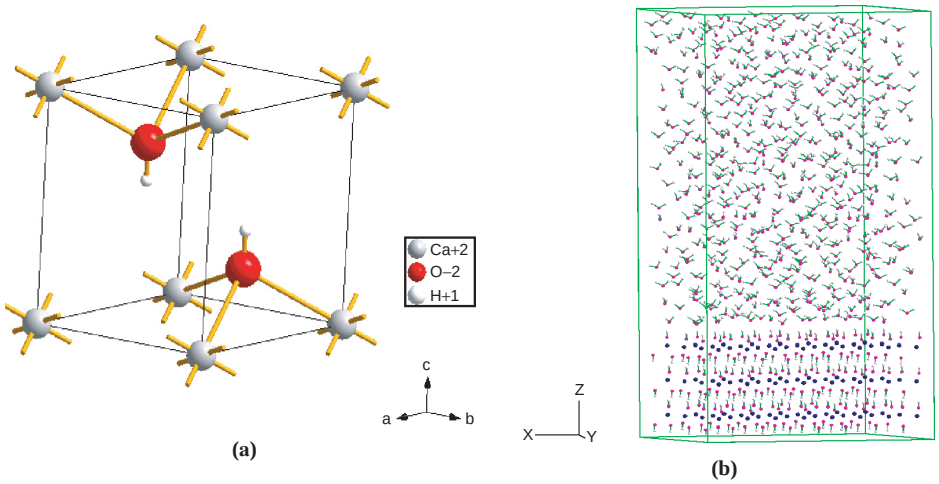

FIGURE 1 Portlandite: (*a*) structure of unit cell and (*b*) MD model of channel.

Tobermorite and Jennite Models

The triclinic hexagonal-shaped unit cell of tobermorite [$Ca_5Si_6O_{16}$-$(OH)_2 \cdot 4H_2O$] is given in Figure 2*a* with side lengths of $a = 11.156$ Å, $b = 7.303$ Å, and $c = 9.566$ Å and angles of $\alpha = 101.08$ degrees, $\beta = 92.83$ degrees, and $\gamma = 89.98$ degrees (*17*). The triclinic hexagonal-shaped unit cell of jennite [$Ca_9Si_6O_{18}(OH)_6 \cdot 8H_2O$] as shown in Figure 2*c* has side lengths of $a = 10.576$ Å, $b = 7.265$ Å, and $c = 10.931$ Å and angles of $\alpha = 101.3°$, $\beta = 96.98°$, and $\gamma = 109.65°$ (*18*). The simulation models for tobermorite and jennite contain $2 \times 2 \times 1$ crystallographic unit cells and $1 \times 4 \times 4$ crystallographic unit cells in the *x*-, *y*-, and *z*-directions as shown in Figure 2*b* and *d*, respectively. Both models simulate the water–solid system at a room temperature of 25°C. A layer of 269 water molecules was imposed above the one layer of unit cells of tobermorite (density 1.574 g/cm^3) to simulate a 25-Å-diameter tobermorite channel filled with porewater. A layer of 541 water molecules was imposed above the four layers of unit cells of jennite (density 1.740 g/cm^3) as shown in Figure 2*d*, which simulates a 40-Å-diameter channel filled with water.

Ettringite Model

The primary AFt phase in cement paste is ettringite [$Ca_3Al(OH)_6 \cdot 12H_2O_2 \cdot (SO_4)_3 \cdot 2H_2O$], which takes the general structure of AFt and was modeled by using MD in this study to represent the generic AFt phase in cement paste. Ettringite is formed during the early hydration of most portland cements with perfect cleavage and can also occur in the natural environment. The unit crystal cell of ettringite (also hexagonal shaped) is shown in Figure 3*a*, with dimensions of $a = b = 11.23$ Å, $c = 21.48$ Å, and angles of $\alpha = \beta = 90°$, and $\gamma = 120°$ (*19*). The simulation model as shown in Figure 3*b* for ettringite contains $2 \times 2 \times 1$ crystallographic unit cells (density of 1.320 g/cm^3) in the *x*-, *y*-, and *z*-directions. This model simulates the water–ettringite system at a room temperature of 25°C. A layer

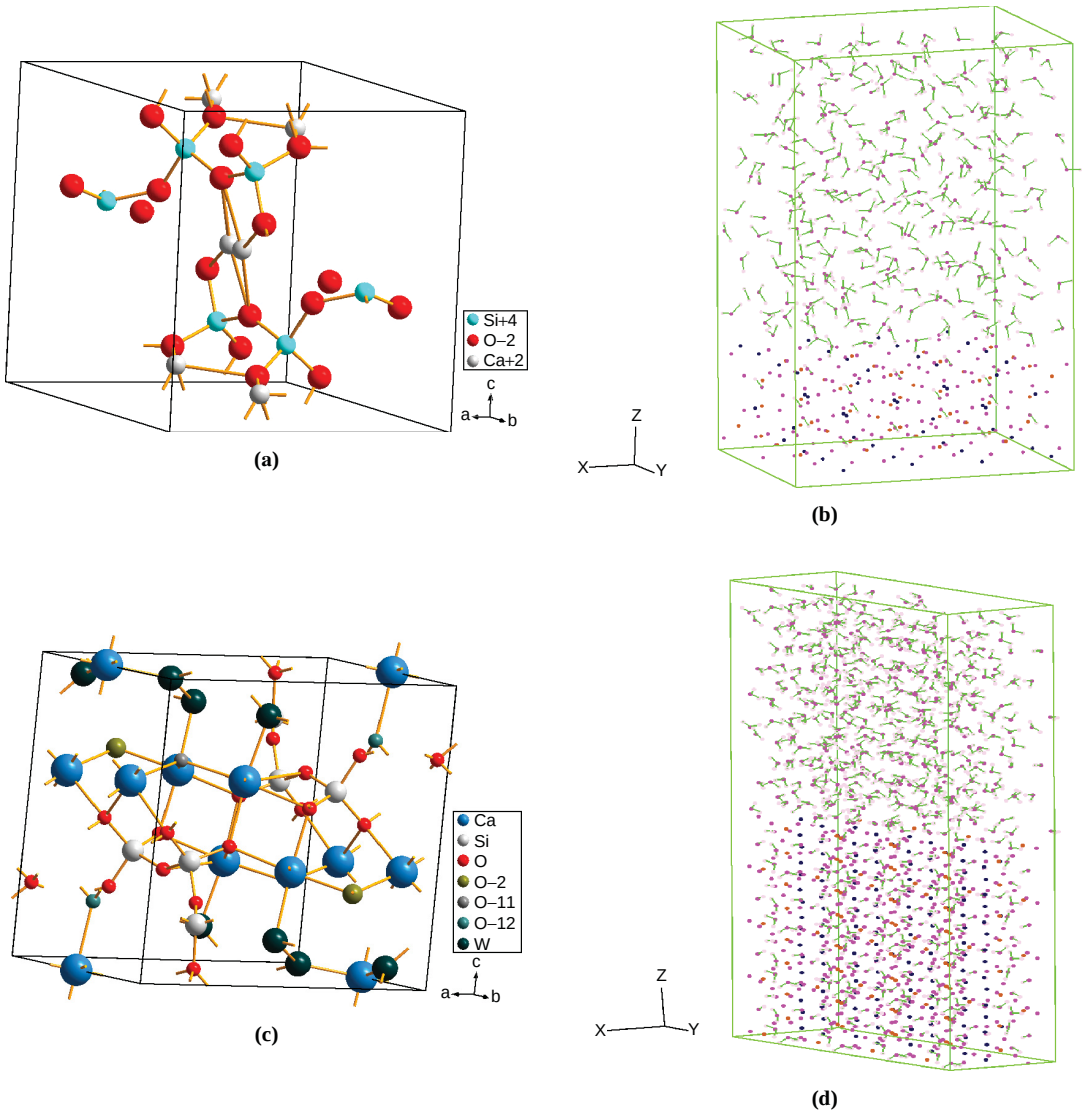

FIGURE 2 Tobermorite: (*a*) structure of unit cell and (*b*) MD model of channel. Jennite: (*c*) structure of unit cell and (*d*) MD model of channel.

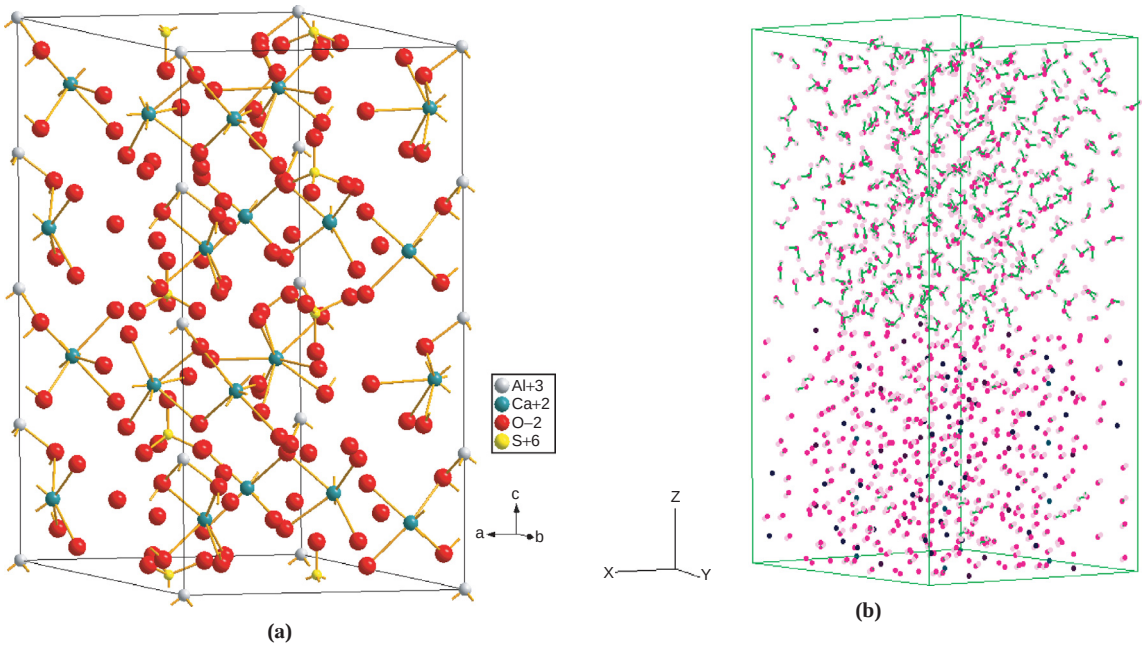

FIGURE 3 Ettringite: (*a*) structure of unit cell and (*b*) MD model of channel.

of 389 water molecules was imposed above the one layer of unit cells of ettringite to simulate a 25-Å-diameter ettringite channel based on the periodic boundary condition.

Hydrocalumite and Kuzelite Models

Hydrocalumite [$Ca_2Al(OH)_6 \cdot Cl \cdot 2H_2O$] is a monoclinic, pseudo-hexagonal crystal with perfect cleavage. Its unit crystal cell has the dimensions $a = 9.979$ Å, $b = 5.751$ Å, $c = 16.320$ Å and angles of $\alpha = 90°$, $\beta = 104.5°$, and $\gamma = 90°$ (*20*) as shown in Figure 4*a*. The sulfate-bearing kuzelite is a platyhexagonal to rhomboidal crystal with perfect cleavage. The unit crystal cell of kuzelite [$Ca_4Al_2(OH)_{12} \cdot SO_4 \cdot 6H_2O$] has the dimensions $a = b = 5.7586$ Å, $c = 26.7946$ Å and angles of $\alpha = \beta = 90°$, and $\gamma = 120°$ (*21*) as shown in Figure 4*c*. The simulation models for hydrocalumite and kuzelite contain, respectively, $2 \times 2 \times 2$ crystallographic unit cells and $4 \times 4 \times 1$ crystallographic unit cells in the *x*-, *y*-, and *z*-directions (Figure 4*b* and *d*). Both models simulate the water–solid system at a temperature of 25°C. A layer of 333 water molecules was modeled above the two layers of unit cells of hydrocalumite (density 1.320 g/cm^3) to simulate a 35-Å-diameter hydrocalumite channel filled with water. A layer of 516 water molecules is imposed above the one layer of unit cells of kuzelite (density 1.767 g/cm^3) as shown in Figure 4*d*, which simulates a 25-Å-diameter kuzelite channel of water.

A canonical situation was run for each model, in which the number of molecules and atoms in a mole (N), volume (V), and temperature (T) are conserved and the energy of endothermic and exothermic processes is exchanged with a thermostat. The temperature T is fixed at 298 K (25°C) for all the models. The parameters of the Lennard–Jones potential function (see Table 1) used in this study were obtained with quantum mechanics and have been used successfully in MD simulations of the same atomic species as those simulated in this study (*22–25*).

Four chloride anions and four sodium cations (to balance the net negative charge of the chloride ions) were included in each model to simulate an NaCl solution with a concentration of 0.3 to 0.5 M. At the beginning of the relaxation stage for each system, all the chloride and sodium ions were positioned at a distance of around 10 Å. For comparison, an MD simulation of one 0.4 M NaCl solution (without hydration solid phases) was performed by using the same set of modeling parameters to obtain the water–species structure at 25°C. A 200-ps (picosecond = 10^{-12} s) analysis was run for each model, following a 20-ps relaxation stage.

VALIDATION OF MD MODELS

The primary objective of the study was to investigate how the various physicochemical interactions between chloride ions and the representative hydration solid compounds influence the transport behavior of the chloride species in the vicinity of these different products. Therefore, an effective validation of the developed MD models can be accomplished by comparing the MD-predicted ionic adsorption with the reliably determined laboratory experimental results such as those obtained from the NMR spectroscopy analyses.

The general pattern of chloride transport in the bulk solution and at the water–solid interface is shown in Figure 5 by two snapshots of MD simulation: Figure 5*a* for the NaCl solution model and Figure 5*b* for the portlandite model. The water molecules in the NaCl solution demonstrated a highly disordered arrangement with an average interatomic distance of about 3.1 Å. In contrast, the very first layer of water molecules on the solid surface of portlandite demonstrated a highly oriented pattern with the oxygen atoms bent toward the hydrogen atoms of the hydroxyls on the solid surface. Of the four chloride anions originally located at the centerline of the portlandite channel, one chloride ion was observed within the H-bond distance from the solid surface and another was vibrating at a distance around 6.5 Å from the surface. One sodium ion showed up at the 10-Å distance from

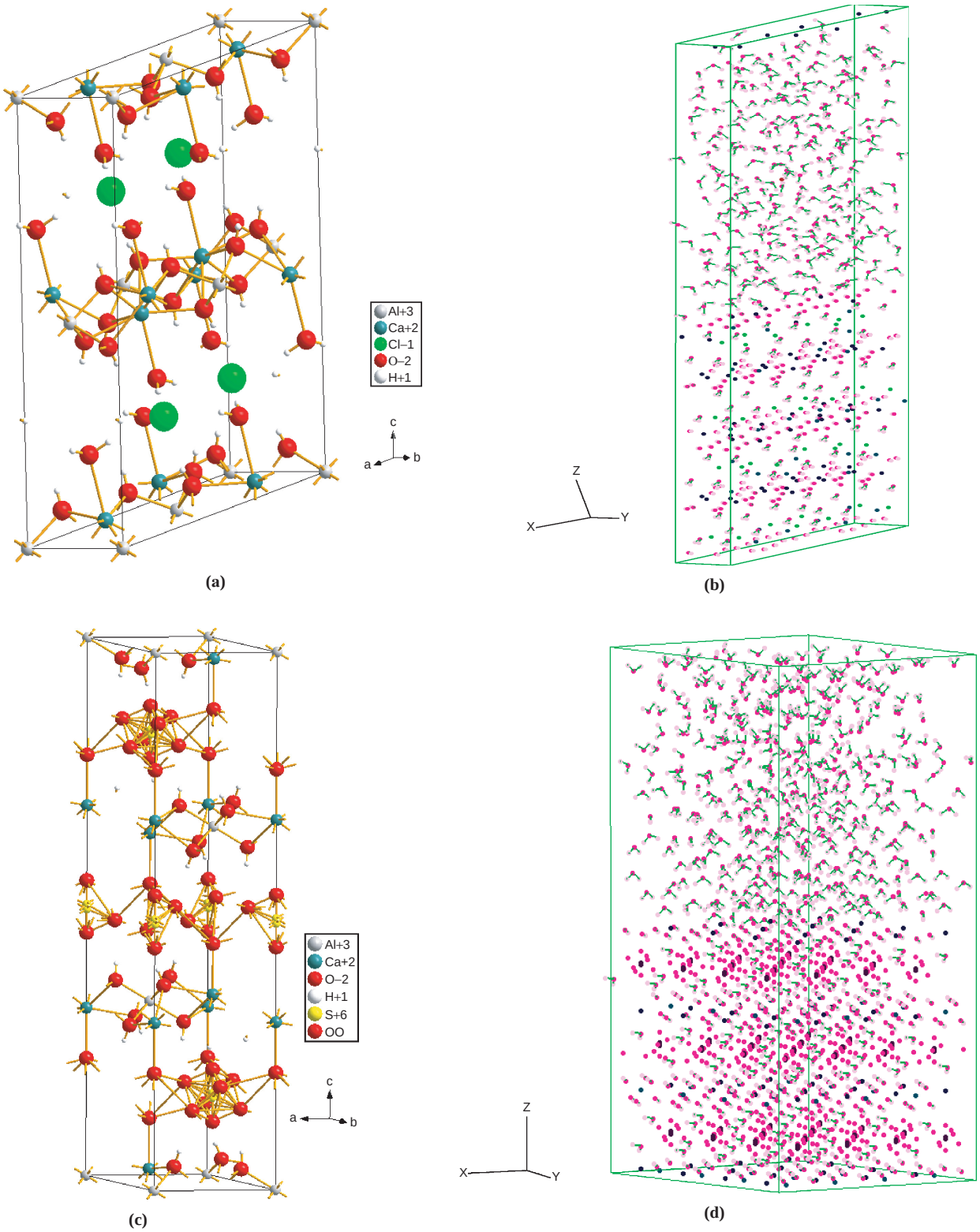

FIGURE 4 Hydrocalumite: (*a*) structure of unit cell and (*b*) MD model of channel. Kuzelite: (*c*) structure of unit cell and (*d*) MD model of channel.

TABLE 1 Parameters of Lennard–Jones Pair Potential Function Used in MD Analyses

Atom 1	Atom 2	$4\epsilon_{12} \cdot \sigma_{12}^{12}$ (kJ · mol^{-1} · Å^{12})	$4\epsilon_{12} \cdot \sigma_{12}^{6}$ (kJ · mol^{-1} · Å^{6})
Si	Na	5.69E+04	8.74E+01
Si	Cl	1.43E+06	4.39E+02
O	Na	5.36E+04	9.46E+01
S	S	1.68E+07	8.37E+03
Ca	Na	2.46E+05	5.40E+01
Al	O	5.31E+04	2.01E+01
Al	Cl	2.69E+05	4.05E+01
Al	Na	1.60E+04	9.87E+00
Al	H	0.00E+00	0.00E+00
Al	Ca	8.58E+03	6.11E–01
Al	Al	8.16E+02	1.35E–01
O w	Al	5.31E+04	2.01E+01
Ca	Cl	2.76E+06	1.81E+02
Cl	O	1.79E+07	6.11E+03
O	O	2.64E+06	2.62E+03
O	Ca	7.03E+05	1.02E+02
Ca	H	0.00E+00	0.00E+00
H	O	0.00E+00	0.00E+00
Ca	O w	7.03E+05	1.02E+02
O	O w	2.64E+06	2.62E+03
S	Na	9.16E+05	1.10E+03
S	Cl	2.06E+07	5.23E+03
S	H	0.00E+00	0.00E+00
S	O	3.39E+06	2.36E+03
S	O w	3.39E+06	2.36E+03
Si	O	2.19E+05	1.92E+02
Si	O w	2.19E+05	1.92E+02
Si	H	0.00E+00	0.00E+00
Si	Ca	5.44E+04	7.20E+00
Si	Si	1.82E+04	1.40E+01
Ca	Ca	7.32E+04	2.48E+00
S	Al	1.23E+05	3.45E+01
Cl	O w	1.79E+07	6.11E+03
S	Ca	1.49E+06	1.67E+02
O w	O w	2.63E+06	2.62E+03
H	H	0.00E+00	0.00E+00
O w	H	0.00E+00	0.00E+00
Na	Na	1.48E+05	4.98E+02
Cl	Na	5.52E+06	3.03E+03
Na	O w	6.65E+05	1.18E+03
Na	H	0.00E+00	0.00E+00
Cl	H	0.00E+00	0.00E+00
Cl	Cl	8.83E+07	1.21E+04

NOTE: O w = water oxygen atom.

the surface. The surface OH groups can be seen to bend toward the chloride ion to allow H-bonding.

In this study, instead of tracking the individual ions, the probability that chloride ions would show up in the specified near-surface spatial domains was calculated to serve the validation purpose. To this end, the aqueous space on the solid surface of each model was divided into two subdomains: one 0- to 3-Å range starting from the solid surface and one 3- to 10-Å range just beyond. The maximum number of chloride ions (out of a total of four) that once simultaneously showed up in each spatial domain and the percentage of time (relative to the total 200-ps evaluation period) each domain was occupied with the different number of ions were monitored for the six hydration compounds as shown in Table 2, which also contains the same information for the sodium species.

The chloride adsorption to the solid surface was then quantified for each domain as the product of the fraction of ions (e.g., ¼ for the <3-Å domain of portlandite) and the corresponding adsorption percent time (e.g., 100% for the ion in the <3-Å domain of portlandite) as given in Table 2. This product is referred to in this study as the MD computed surface-adsorbed fraction of the chloride in each different domain (e.g., 25% as the product of ¼ and 100% for the <3-Å domain of portlandite). The MD-computed surface-adsorbed fractions for both chloride and sodium species were then compared with the surface-adsorbed fraction results obtained from the NMR experiments.

The series of ^{35}Cl-NMR and ^{23}Na-NMR experiments conducted in this study included a NaCl solution and six solid–solution suspensions. Each solid–solution suspension was prepared by mixing one of the six solid hydration compounds with a NaCl solution with the same Cl^- concentration used in the corresponding MD simulation. The NMR surface-adsorbed fractions of the chloride and sodium species were determined by using a two-site exchange model expressed in Equation 11, which was developed on the basis of the data of the spin-lattice relaxation time T_1 from the NMR analyses (*26*). The time difference, ΔT_1, between the spin-lattice relaxation time T_1 of the chloride or sodium ions in the neat NaCl solution and the T_1 of the chloride or sodium ions in a suspension measures the fraction of adsorbed ions by the solid surface in the suspension.

$$\frac{1}{T_{1\text{-sus}}} = \frac{(1-\alpha)}{T_{1\text{-sol}}} + \frac{\alpha}{T_{1\text{-ads}}} \tag{11}$$

where

$T_{1\text{-sus}}$ = spin-lattice relaxation time of suspension,
$T_{1\text{-sol}}$ = spin-lattice time of neat NaCl solution (without solid hydration compound),
$T_{1\text{-ads}}$ = spin-lattice time of adsorbed species, and
α = adsorbed fraction of chloride or sodium species.

$T_{1\text{-sus}}$ and $T_{1\text{-sol}}$ were measured in the NMR experiments, whereas $T_{1\text{-ads}}$ was determined by extrapolation to extreme dilution at $\alpha = 1$. With the values of the $T_{1\text{-sus}}$, $T_{1\text{-sol}}$, and $T_{1\text{-ads}}$, the α-values, as the bound fractions of chloride or sodium by the solid surface, were finally determined for the six hydration compounds.

The MD-computed surface-adsorbed fractions of the chloride ions in the 3-Å domain and 3- to 10-Å domain on the solid surface were both significantly smaller than the NMR-measured α based on the two-site exchange model, whereas the MD-computed cumulative adsorbed fraction of chloride ions of these two domains, or the 0- to 10-Å domain, showed excellent agreement with the NMR results for all six models (Figure 6). The slightly lower predictions (within 5%) by the MD models could be attributed to the trivial binding effects of the solid surface on the chloride ions positioned beyond the 10-Å distance from the surface that was not included in the MD-computed surface-adsorbed fractions.

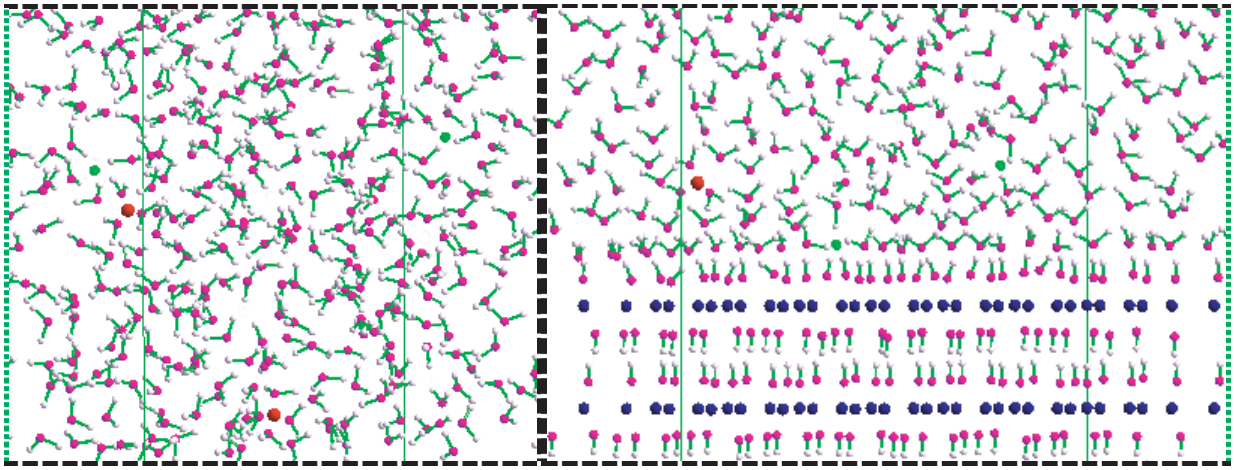

(a) (b)

FIGURE 5 Cl^- (green and smaller) and Na^+ (red and bigger) (*a*) in NaCl solution and (*b*) on portlandite surface.

QUANTIFICATION OF CHLORIDE DIFFUSION IN HYDRATED PHASES

On the basis of the trajectory outputs of the chloride and sodium ions from the 200-ps MD simulations, the coefficient of effective diffusion D (D in equilibrium diffusion) was computed for the two species in the different spatial domains on the solid surface of each hydration compound by using the mean-square displacement (MSD) formula (*27*). The MSD values for the chloride and sodium species were calculated according to Equation 12 by preparing time-series data items of length Δt (0.1 fs in this study), and averaging the data items on the basis of the number of ions of each species.

$$\text{MSD} = \frac{1}{NM}\sum_{i}^{N}\sum_{k}^{M}\left\langle \left\| r_i\left(t_k + \Delta t\right) - r_i\left(t_k\right)\right\| \right\rangle^2 \tag{12}$$

where

M = number of time series,
N = number of ions,
r_i = location of ion i, and
t_k = starting time of kth time series.

From the computed MSD, diffusion coefficient D was determined by using Einstein's equation as follows (Equation 13). A 200-ps running period was found to be long enough for all six MD models, as shown in Figure 7 by the linear MSD for chloride ions (<3 Å from the solid surface) in the ettringite model. The diffusion coefficients D of the chloride and sodium ions were computed for all six systems in the different domains (<3 Å, 3 to 10 Å, >10 Å) on the solid surface (Table 3). The D-value of a domain given in Table 3 was computed for the ion or ions showing up in the domain, with consideration of the percent time that the domain was occupied by the ion.

$$D = \lim_{t\to\infty}\frac{1}{6t}\text{MSD} \tag{13}$$

DISCUSSION OF RESULTS

On average, the MD-computed diffusion coefficients of chloride and sodium in the near-surface domain (less than 10 Å from the solid surface) are about one order of magnitude greater than those measured experimentally in cement paste samples (usually of 10^{-11}-m^2/s magnitude). The primary reason for the difference is the morpholog-

TABLE 2 Adsorption of Chloride and Sodium Ions to Surface of Hydration Compounds

Ingress Species	Distance from Solid Surface (Å)	Hydration Phase					
		Portlandite	Tobermorite	Jennite	Ettringite	Hydrocalumite	Kuzelite
Cl^-	<3	1/4 (100%)	0/4 (N/A)	0/4 (N/A)	1/4[a] (48%)	2/4 (81%, 100%)[b]	2/4 (38%, 100%)
	3–10	1/4 (100%)	0/4 (N/A)	0/4 (N/A)	2/4 (52%, 100%)	2/4 (19%, 100%)	2/4 (62%, 100%)
Na^+	<3	0/4 (N/A)	1/4 (100%)	1/4 (100%)	1/4 (100%)	0/4 (N/A)	0/4 (N/A)
	3–10	1/4 (95%)	2/4 (95%, 100%)	2/4 (88%, 100%)	2/4 (85%, 100%)	0/4 (N/A)	0/4 (N/A)

NOTE: N/A = not applicable. Values indicate maximum number of chloride or sodium ions (from a total of four) that simultaneously showed up in each domain and percentage of time each domain was occupied with the ions.
[a]One chloride ion was observed in the 3 Å domain, forming temporary H-bond with the surface hydroxyls.
[b]The <3 Å domain on hydrocalumite surface is 81% time occupied with two Cl^-, 100% time with at least one.

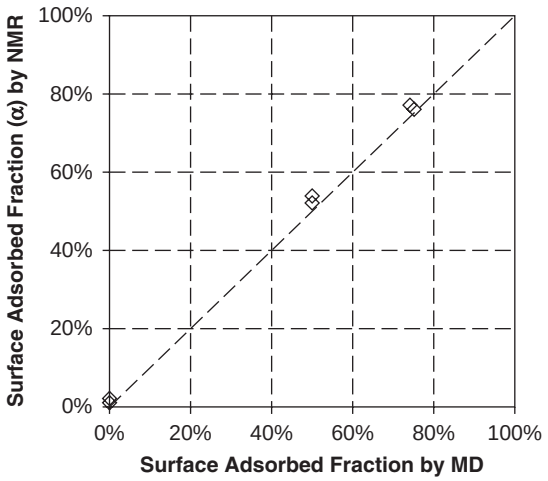

FIGURE 6 MD-predicted surface-adsorbed fraction of chloride ions (0 to 10 Å) versus NMR results.

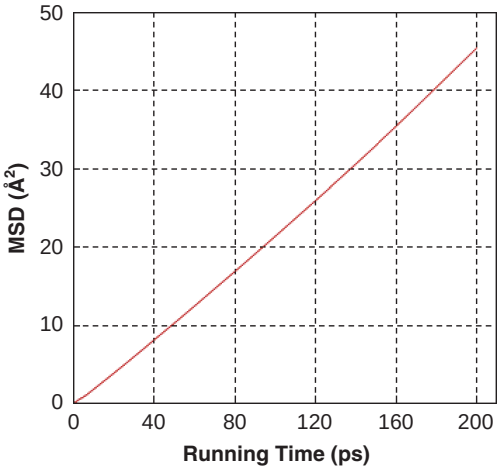

FIGURE 7 MSD of chloride ions on surface of ettringite (<3 Å).

ical tortuosity effect of the microscopic channels and interconnected pores in hydrated cement paste, which could significantly increase the distance for ions to travel in cement paste. From the MD simulations conducted in this study, the mechanism of reinforcement corrosion due to localized chloride concentration can be reasonably explained. The computed diffusion coefficients of chloride in the near-surface domains (less than 10 Å from the solid surface) vary pretty much on the surface of the different hydration phases. The difference in the transport rates of chloride ions could be further enhanced by tortuosity effects of one more order of magnitude, considering that microscopic channels and pores are usually more tortuous than macroscopic ones. Cement paste usually contains pores of very different sizes, from gel pores of subnano or nano scale to entrapped air bubbles as large as 3 mm; therefore the transport velocity of chloride may vary up to two orders of magnitude at different locations within a concrete matrix. The different transport rates of chloride ions would in turn result in a highly heterogeneous chloride concentration in the same concrete structure.

SUMMARY AND CONCLUSIONS

Understanding the physicochemical interactions among the ionic species, water molecules, and the solid surface of hydration products is critical to preventing reinforcement corrosion due to concentrated chloride in the concrete of transportation infrastructure. Solid surfaces of the hydration products significantly influence the dynamics of chloride ions in two major mechanisms: the presence of electrostatic fields and the local surface-specific H-bonding acceptation. A well-developed H-bonding network is generally formed between the water molecules and the solid surface of the hydration products, which plays an important role in the interactions of chloride ions with the solid hydration phases. The two AFm phases, hydrocalumite or kuzelite, showed the strongest chloride-binding capacity in the MD simulations owing to the cumulative effects of its structural positive charge and the H-bonding between chloride ions and surface hydroxyls.

Chloride ions also demonstrated quite strong adsorption to the surface of portlandite; however, the adsorption was maintained only through H-bonding. With negatively charged oxygen atoms on its surface, the AFt-phase ettringite demonstrated a lower chloride-binding capacity compared with portlandite. The C-S-H phases, tobermorite and jennite, with bare oxygen atoms from their surface Si-O^- sites, did not show a detectable binding effect on chloride ions. The sodium-binding capacities of the six hydration compounds show a generally opposite trend to their chloride-binding capacities. The effective diffusion coefficients of chloride and sodium were computed at different distances from the solid surface. The migration rates of the chloride and sodium ions were found to be highly dependent on the positions where they showed up on the solid surface and the adsorption capabilities the solid surface demonstrated to them.

TABLE 3 MD-Computed Diffusion Coefficients (10^{-10} m^2/s) on Surface of Different Compounds

Ingress Species	Distance from Solid Surface (Å)	Hydration Phase					
		Portlandite	Tobermorite	Jennite	Ettringite	Hydrocalumite	Kuzelite
Cl^-	<3	3.72	N/A[a]	N/A	3.42[b]	1.84	2.16
	3–10	16.23	N/A	N/A	8.12	9.28	10.59
	>10	22.69	23.34	23.67	22.83	22.16	22.51
Na^+	<3	N/A	0.83	0.95	0.98	N/A	N/A
	3–10	5.13	3.52	3.67	4.11	N/A	N/A
	>10	8.35	8.02	8.06	9.16	9.61	9.55

[a]N/A (not available) means no chloride or sodium ions were observed in MD simulations.
[b]*D* value was computed for the chloride ion based on the time it stayed within the 3 Å distance.

REFERENCES

1. Pan, T., T. A. Nguyen, and X. Shi. Assessment of Electrical Injection of Corrosion Inhibitor for Corrosion Protection of Reinforced Concrete. In *Transportation Research Record: Journal of the Transportation Research Board, No. 2044*, Transportation Research Board of the National Academies, Washington, D.C., 2008, pp. 51–60.
2. Basheer, L., J. Kropp, and D. J. Cleland. Assessment of the Durability of Concrete from Its Permeation Properties. *Construction and Building Materials*, Vol. 15, 2001, pp. 93–113.
3. Xi, Y., K. Willam, and D. Frangopol. Multiscale Modeling of Interactive Diffusion Process in Concrete. *Journal of Materials in Civil Engineering*, ASCE, Vol. 126, No. 3, 2000, pp. 258–265.
4. Russell, H. G. *NCHRP Synthesis of Highway Practice 333: Concrete Bridge Deck Performance*. Transportation Research Board of the National Academies, Washington, D.C., 2004.
5. Luping, T., and L. O. Nilsson. Rapid Determination of Chloride Diffusivity in Concrete by Applying an Electric Field. *ACI Materials Journal*, Vol. 49, No. 1, 1992, pp. 49–53.
6. Gmira, A. M., R. J. Zabat, M. Pellenq, and H. Van Damme. Microscopic Physical Basis of the Poromechanical Behavior of Cement-Based Materials. *Materials and Structures*, Vol. 37, No. 1, 2004.
7. Kalinichev, A. G., and R. J. Kirkpatrick. Molecular Dynamics Modeling of Chloride Binding to the Surfaces of Calcium Hydroxide, Hydrated Calcium Aluminate, and Calcium Silicate Phases. *Chemistry of Materials*, Vol. 14, 2002, pp. 3539–3549.
8. Alder, B. J., and T. E. Wainwright. Phase Transition for a Hard-Sphere System. *Journal of Chemical Physics*, Vol. 27, 1957.
9. Alder, B. J., and T. E. Wainwright. Studies in Molecular Dynamics: I. General Method. *Journal of Chemical Physics*, Vol. 31, 1959, pp. 459–466.
10. Rahman, A. Correlations in the Motion of Atoms in Liquid Argon. *Physics Review Letters*, Vol. 136, 1964, pp. A405–A411.
11. Stillinger, F. H., and A. Rahman. Improved Simulation of Liquid Water by Molecular Dynamics. *Journal of Chemical Physics*, Vol. 60, 1974, pp. 1545–1557.
12. Beeman, D. Some Multistep Methods for Use in Molecular Dynamics Calculations. *Journal of Computational Physics*, Vol. 20, 1976, pp. 130–139.
13. Taylor, H. F. W. *Cement Chemistry*, 2nd ed. Thomas Telford, London, 1997.
14. Sparks, D. L., and T. J. Grundl. *Mineral-Water Interfacial Reactions*. ACS Symposium Series 715. American Chemical Society, Washington, D.C., 1998.
15. Petch, H. E. The Hydrogen Positions in Portlandite, $Ca(OH)_2$, as Indicated by the Electron Distribution. *Acta Crystallographica*, Vol. 14, 1961, pp. 950–957.
16. Allen, M. P., and D. J. Tildesley. *Computer Simulation of Liquids*. Oxford University Press, New York, 1987.
17. Merlino, S., E. Bonaccorsi, and T. Armbruster. Tobermorites: Their Real Structure and Order-Disorder (OD) Character. *American Mineralogist*, Vol. 84, 1999, pp. 1613–1621.
18. Bonaccorsi, E., S. Merlino, and H. F. W. Taylor. The Crystal Structure of Jennite, $Ca_9Si_6O_{18}(OH)_6*8H_2O$. *Cement and Concrete Research*, Vol. 34, 2004, pp. 1481–1488.
19. Moore, A. E., and H. F. W. Taylor. Crystal Structure of Ettringite. *Acta Crystallographica*, Vol. B26, 1970, pp. 386–393.
20. Sacerdoti, M., and E. Passaglia. Hydrocalumite from Latium, Italy: Its Crystal Structure and Relationship with Related Synthetic Phases. *Neues Jahrbuch für Mineralogie-Monatshefte*, 1988, pp. 462–475.
21. Allmann, R. Refinement of the Hybrid Layer Structure $(Ca_2Al(OH)_6)*(1/2SO_4*3H_2O)$. *Neues Jahrbuch für Mineralogie-Monatshefte*, 1977, pp. 136–144.
22. Wang, J., A. G. Kalinichev, R. J. Kirkpatrick, and R. T. Cygan. Structure, Energetics, and Dynamics of Water Adsorbed on the Muscovite (001) Surface: A Molecular Dynamics Simulation. *Journal of Physical Chemistry B*, Vol. 109, No. 33, 2005, pp. 15893–15905.
23. Berendsen, H. J. C., J. P. M. Postma, W. F. van Gunsteren, and J. Hermans. Interaction Models for Water in Relation to Protein Hydration. *Nature*, Vol. 224, 1969, pp. 175–177.
24. Dang, L. X. Mechanism and Thermodynamics of Ion Selectivity in Aqueous Solutions of 18-Crown-6 Ether: A Molecular Dynamics Study. *Journal of the American Chemical Society*, Vol. 117, 1995, pp. 6954–6960.
25. Cannon, W. R., B. M. Pettitt, and J. A. McCammon. Sulfate Anion in Water: Model Structural, Thermodynamic and Dynamic Properties. *Journal of Physical Chemistry*, Vol. 98, 1994, pp. 6225–6230.
26. Yu, P., and R. J. Kirkpatrick. ^{35}Cl NMR Relaxation Study of Cement Hydrate Suspensions. *Cement and Concrete Research*, Vol. 31, 2001, pp. 1479–1485.
27. Allen, M. P., and D. J. Tildesley. *Computer Simulation of Liquids*. Oxford University Press, New York, 1987.

The Nanotechnology-Based Concrete Materials Task Force sponsored publication of this paper.